High Power Laser Science and Engineering, (2025), Vol. 13, e23, 9 pages.
doi:10.1017/hpl.2025.8

HIGH POWER LASER SCIENCE AND ENGINEERING

RESEARCH ARTICLE

High-power microsecond ultraviolet burst-mode pulse laser with a rectangular envelope and GHz-adjustable intra-burst pulses

Yanran Gu[1,2], Xinyue Niu[1,2], Fuyin Liu[1,2], Ting He[1,2], Jinmei Yao[1,2], Muyu Yi[1,2], Langning Wang[1,2], Tao Xun[1,2], and Jinliang Liu[1,2]

[1]*College of Advanced Interdisciplinary Studies, National University of Defense Technology, Changsha, China*

[2]*Nanhu Laser Laboratory, National University of Defense Technology, Changsha, China*

(Received 29 October 2024; revised 29 December 2024; accepted 14 January 2025)

Abstract

We demonstrate a high-peak-power master oscillator power amplifier burst-mode laser system that generates microsecond burst duration pulses at 355 nm with a GHz-adjustable intra-burst pulse frequency. In the fiber seed, a high-bandwidth electro-optic modulator is employed to modulate a continuous-wave (CW) laser into a pulse train at GHz frequency. To acquire a microsecond rectangular burst pulse envelope, two acousto-optic modulators are used to chop the CW pulse train and generate a pre-compensation burst envelope. A three-stage neodymium-doped yttrium aluminum garnet amplifier boosts the burst-mode fiber seed's burst energy of 1.65 J at 1064 nm. To achieve a high-power ultraviolet (UV) burst-mode laser, sum frequency generation in a LiB_3O_5 crystal is employed to convert the wavelength, achieving over 300 kW of peak power at 1.15 μs/10 Hz. The intra-burst pulse frequency of the UV burst laser can be adjustable from 1 to 10 GHz with a sinusoidal waveform. To the best of our knowledge, this paper represents the highest reported microsecond UV burst-mode laser in terms of output energy and peak power with the GHz-adjustable intra-burst frequency. The high-power microsecond UV burst-mode pulse laser can be directly used as a light-driven source in large-bandwidth/high-power microwave photonic systems, providing a long pulse width and high peak power laser while significantly improving the system's multi-parameter adjustment capability and adaptability.

Keywords: adjustable intra-burst pulse; burst-mode laser; photoconductive semiconductor switches; ultraviolet pulse laser

1. Introduction

Burst-mode lasers combine a series of closely spaced pulses into short bursts to achieve high peak power and high repetition rate. This property allows them to be used in a wide range of applications, such as certain material micro-machining[1,2], medicine[3,4] and scientific research[5,6]. Recently, a novel application has involved employing high-peak-power tunable radio-frequency (RF; GHz) burst-mode lasers to illuminate the photoconductive semiconductor switches (PCSSs) to generate high-power, GHz frequency-agile RF/microwaves (photoconductive microwave technology, PMT)[7–10], where the burst-mode lasers are used as the optical drive source of the PMT, in which the characteristics of burst-mode lasers can influence the properties of the microwave. The intra-burst pulse frequency of the burst-mode lasers determines the bandwidth of the microwave. The high peak power of the burst-mode laser can significantly lower the on-resistance of the PCSS, which is beneficial for generating high-power microwave signals, and a 355 nm laser can activate the intrinsic absorption of the PCSS (SiC, GaN, etc.) to increase its light absorption efficiency[11,12]. Ref. [13] shows that a 355 nm laser can achieve photocurrent output up to 15 times greater than a 1064 nm laser for PCSS (SiC) triggering. Currently, there are two primary methods for generating microwaves. The first method relies on pure electric microwave technology, which is the main approach for generating high-power microwaves. However, this method faces limitations in achieving a wide frequency tuning range and bandwidth at high frequencies (~GHz) due to inherent physical principles[14–16]. The second method involves

Correspondence to: T. Xun, College of Advanced Interdisciplinary Studies, National University of Defense Technology, Changsha 410073, China. Email: xuntao@nudt.edu.cn

microwave photonic (MWP) technology[17,18], which utilizes modulated lasers to illuminate photoelectric converters to generate large-bandwidth microwave signals. However, since this approach often employs photodiodes (PDs) as photoelectric converters, it is difficult to achieve high-power microwave output. The PMT combines the advantages of pure electric microwave technology and MWP technology. It can generate high-power (~kW) and tunable wide bandwidth (~GHz) microwaves[13,19]. These features of wide bandwidth and high power make PMT suitable for high-power microwave applications, particularly for high-power MWP radar applications. To adapt the burst-mode laser to be suitable for high-power MWP radar applications, in addition to high-peak-power and ultraviolet (UV) wavelength characteristics, some key parameters for pulsed cluster lasers need to be considered. Firstly, a long pulse duration (~μs) is advantageous for enhancing the radar's detection distance. In addition, a wide adjustable range of intra-burst pulse frequencies can improve detection precision and enable the radar to function in multiple operational modes[20]. The rectangular envelope of microwave waveforms enhances the effective detection time of radar. Therefore, a high-peak-power UV wavelength burst-mode laser with a microsecond rectangular envelope and a GHz-adjustable intra-burst pulse frequency is needed.

In 2013, Huang *et al.*[21] reported a picosecond UV burst-mode amplifier that had a macro-pulse burst duration of 10 μs and a micro-pulse width of 66 ps. The 355 nm laser system provided tunable macro-pulse durations of 5 and 10 μs by using an electro-optic modulator (EOM). Although the burst-mode laser achieved a maximum burst energy of 135 mJ at a 10 μs near-flat-top envelope by modulating the shape of the macro-pulse envelope, intra-burst pulse frequency adjustability was not demonstrated. In 2023, Zhang *et al.*[22] reported a frequency quadrupling microsecond burst-mode laser operating at 16 μs macro-pulse duration. The 266 nm laser system delivered a micro-pulse energy of 135 nJ with a micro-pulse width of 18 ps at a repetition rate of 178 MHz. By precisely controlling the delay between the front edges of macro-pulses and pump pulses, a flat-top amplified macro-pulse envelope was successfully achieved. However, this laser system micro-pulse frequency tunability was not characterized. In addition, with the peak power of the laser it was difficult to generate microwave signal[23]. Recently, our research group preliminarily developed a 1064 nm microsecond burst-mode fiber seed source[24]. The pulse duration of the laser was 5.5 μs with an intra-burst pulse adjustable frequency range of 1–2 GHz using a high-bandwidth EOM. The output burst energy of the fiber seed was 26.6 μJ, resulting in a peak power of approximately 10 W. With the peak power of the laser it was difficult to trigger the PCSS-generated microwave signal. Currently, there have been few studies on high-power microsecond UV burst-mode lasers designed for high-power MWP radar applications. Most UV burst-mode pulse laser systems use a master oscillator power amplifier (MOPA) configuration to provide flexibility of the pulse parameters. This setup includes a burst-mode pulse fiber seed, a neodymium-doped yttrium aluminum garnet (Nd:YAG) energy amplifier and a third harmonic generator (THG), where the fiber seed provides multi-parameter tunable parameters, the Nd:YAG amplifier amplifies the energy of the fiber seed and the wavelength conversion part is used to efficiently convert the 1064 nm laser to 355 nm. To achieve a microsecond burst-mode pulse fiber laser with flexible pulse parameters, several methods can be applied. One approach involves employing a mode-locked fiber laser that is modulated by a *Q*-switch that periodically cuts off the microsecond pulse train[25–27]. However, because of the complex structure of the mode-locked laser, it is difficult to achieve a wide range of GHz tuning. Another method to achieve a high frequency for the intra-burst pulse involves employing a fiber frequency multiplier[28,29]. This method can generate a high-frequency burst-mode laser by multiple fiber doubling, but generating a tunable intra-burst parameter is difficult for the fixed amplifier structure. One option is to employ an EOM to generate a tunable parameter over GHz frequency. However, the power of the seed laser is limited by the power capacity of the EOM, which often necessitates the use of multi-stage amplification to boost the energy of the seed laser. During this process, two primary challenges are encountered: the impact of amplified spontaneous emission (ASE) and the waveform distortion caused by gain saturation effects, which are particularly severe when amplifying microsecond pulses. Therefore, meticulously designing the structure of optical fibers and Nd:YAG amplifiers is crucial for effectively suppressing ASE and reducing the waveform.

In this paper, we demonstrate a high-power UV burst-mode pulse laser based on MOPA configuration. The laser system has a microsecond burst duration and a GHz tunable intra-burst pulse frequency. First of all, to achieve flexible parameters and an adjustable burst-mode fiber seed, we employ a large-bandwidth EOM to convert a continuous-wave (CW) laser into a sinusoidal pulse train, with an adjustable frequency ranging from 1 to 10 GHz. In addition, two acousto-optic modulators (AOMs) are utilized for pulse picking and waveform compensation, resulting in a burst-mode pulse laser with a duration of 1.1 μs at a repetition rate of 10 Hz. Secondly, a multi-stage Nd:YAG amplifier is designed to increase the burst energy of the burst-mode fiber seed to 1.65 J, corresponding to a peak power of 3.3 MW. Finally, high-efficiency sum frequency generation (SFG) parts are employed to achieve a peak power exceeding 300 kW for the UV laser. The high-power UV burst-mode laser exhibits a burst duration of 1.15 μs with a nearly rectangular envelope. To the best of our knowledge, this paper represents the highest reported microsecond UV burst-mode laser in terms of output energy and peak power with a

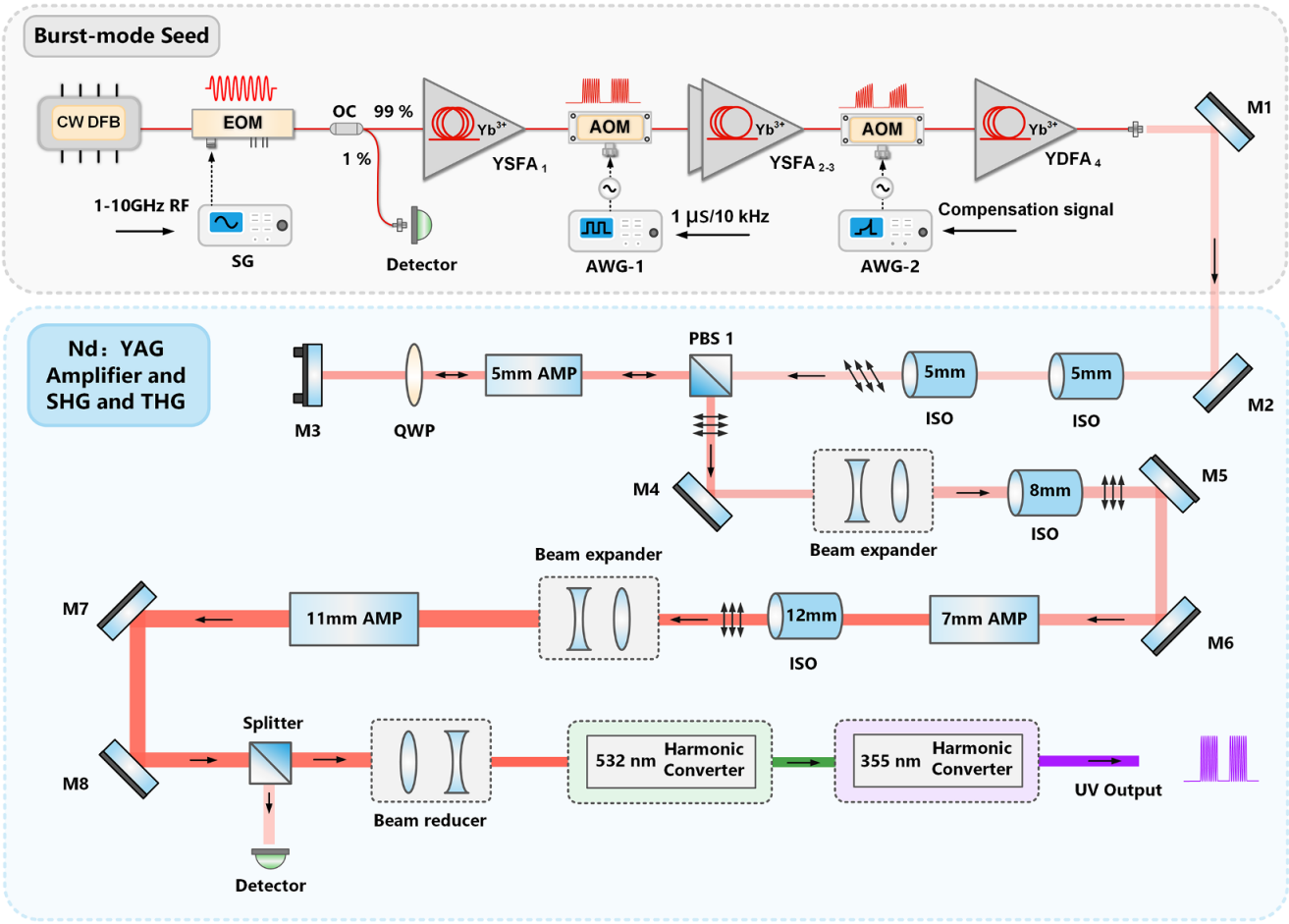

Figure 1. Schematic diagram of the high-power UV burst-mode pulse laser system. CW, continuous-wave; DFB, distributed feedback laser; EOM, electro-optic modulator; SG, signal generator; OC, optical coupler; AOM, acousto-optic modulator; YDFA, ytterbium-doped fiber amplifier; AWG, arbitrary waveform generator; M1–M8, mirrors 1–8; QWP, quarter-wave plate; PBS, polarization beam splitter; Amp, Nd:YAG amplifier.

GHz-adjustable intra-burst frequency. The high-peak-power microsecond UV burst-mode pulse laser can be directly used as an efficient light-driven source in large-bandwidth/high-power MWP systems, providing a long pulse width and high-peak-power laser while significantly improving the system's multi-parameter adjustment capability and adaptability.

2. Experimental setup

The high-power UV burst-mode laser system setup is illustrated in Figure 1. It consists of three primary sections: a burst-mode fiber seed, a multi-stage Nd:YAG amplifier and a wavelength conversion component. The burst-mode fiber seed is a 1064 nm narrow-linewidth laser, which consists of five parts: a CW seed source, a high-frequency modulator, a pulse chopped module, a waveform compensation part and a main fiber amplifier. The CW seed source is a polarization-maintaining (PM) 1064 nm distributed feedback (DFB) laser with a linewidth of 0.04 nm. An isolator (ISO) is used to protect the DFB laser from optical feedback generated from the rest of the laser amplifier chains. The high-frequency modulation uses an EOM with 3.5 dB insertion loss and 10 GHz bandwidth to modulate the CW seed laser into a GHz pulse train. It is worth noting that the EOM is under the control of a signal generator (SG; Sinolink Technologies, SLFS24A) and a direct-current (DC) bias controller. The DC bias controller voltage is approximately 4 V. It needs to be matched to the EOM half-wave voltage to prevent distortion of the signal. The stage of a PM CW Yb^{3+}-doped single-mode fiber amplifier ($YSFA_1$) is incorporated into the system to compensate for the energy loss caused by the EOM. The optical fiber coupler (OC) has a 1:99 coupling ratio, with the 1% port serving to monitor the frequency characteristics of the pulse train.

A high extinction ratio AOM-1 (extinction ratio > 20 dB) with a maximum bandwidth of 200 MHz is employed to chop the pulse train into a microsecond burst-mode pulse laser, where an arbitrary waveform generator (AWG-1) generates 10 kHz rectangular pulse program to AOM-1, which chops the pulse train into a burst-mode laser with a burst duration of 1.15 μs and a repetition rate of 10 kHz. It is worth noting that AOM-1 chops the pulse trains at 1.1 μs/10 kHz and the

resulting macro-pulse duty cycle is 1%, providing sufficient energy for fiber amplification after chopping and alleviating waveform distortion in subsequent amplification. Then, a two-stage PM $YSFA_{2–3}$ is used for energy compensation. The waveform compensation section comprises AWG-2 and AOM-2. AWG-2 generates a pulse program with a low front and high back at 10 Hz, which is sent to AOM-2 to compensate for the gain saturation effects caused by subsequent energy amplification. In addition, it adjusts the pulse repetition rate of the burst-mode laser from 10 kHz down to 10 Hz. A bandpass filter with a 2 nm pass bandwidth is set at each stage of fiber amplification to further suppress ASE in the frequency domain and isolate any reverse return light. The burst-mode seed is amplified by a main fiber amplifier stage ($YSFA_4$). The primary fiber amplifier comprises a 1.3-m Yb^{3+}-doped double-clad PM fiber, featuring core and cladding diameters of 10 and 125 μm, respectively, and exhibiting an absorption coefficient of 4.8 dB/m at 976 nm. It is powered by a 976 nm laser diode (LD) capable of delivering a maximum average power of 6 W. The burst-mode seed laser and pump lasers are injected into the gain fiber using a $(2 + 1) \times 1$ signal–pump combiner. All components of the fiber amplifier are polarization-maintained to maintain the polarization characteristics of the fiber laser. To reduce cladding light and suppress backward reflections, a home-made fiber endcap with a cladding light stripper (CLS) is spliced directly onto the gain fiber. Considering that the system operates at a rather low repetition rate of 10 Hz, synchronous pulse pumping technology is applied in the main amplifier stages to reduce the ASE. A digital delay generator (Stanford Research Systems, DG645) is employed to control the time series of the whole amplifier system.

The multi-stage Nd:YAG amplifier is a customized amplifier system consisting of three amplification stages with Nd:YAG heads having diameters of 5, 7 and 11 mm. The 5 mm diameter Nd:YAG amplifier stage is a double-pass amplifier structure used to increase the energy of the burst-mode fiber seed. Firstly, the collimated burst-mode fiber laser passes through two 5 mm diameter Faraday ISOs before entering the amplifiers. These ISOs not only prevent potential damage to the fiber seed caused by reflected light but also adjust the polarization state of the burst-mode fiber seed laser. The fiber laser output from the ISOs is amplified by a 5 mm diameter double-pass Nd:YAG amplifier. The amplified laser beam exiting the polarization beam splitter (PBS) then passes through a beam expander system to increase its diameter to approximately 7 mm. This increase in diameter is beneficial for improving the amplification efficiency in the 7 mm diameter Nd:YAG amplification stage. Next, an ISO of diameter of 8 mm is used to suppress ASE and prevent the influence of reflected light on the 5 mm diameter Nd:YAG amplifier. After passing through the 8 mm diameter ISO, the laser beam is reflected by the combination of M5 and M6 and enters the 7 mm diameter Nd:YAG rod for amplification. Following the 7 mm diameter Nd:YAG amplification stage, the laser beam passes through a further 12 mm diameter ISO to prevent back-reflected lasers and suppress ASE. Subsequently, a beam expander system is placed after the 12 mm diameter ISO to expand the laser beam to about 11 mm to match the size of the 11 mm diameter Nd:YAG amplification stage. In addition, this beam expansion helps reduce the risk of potential damage to the components in the subsequent stage. The expanded laser beam then enters the 11 mm diameter Nd:YAG amplification stage for further amplification. The amplified laser beam is reflected by M7 and M8 before entering a 1:99% beam splitter. Of the laser output, 1% is directed for energy monitoring, while the remaining 99% is injected into a wavelength conversion component. It is worth noting that each amplification stage in the system comprises two YAG rods and is sandwiched between two optical components: a negative lens designed to counteract thermal lensing effects in the rod heads and a quartz rotator that mitigates the thermal birefringence generated by the rods. In addition, the angles of the components in each amplification stage are carefully designed to minimize the potential for self-oscillation during the amplification process. At the end of the laser system, to improve the wavelength conversion efficiency of the system, the 1064 nm high-power burst-mode laser is introduced into the wavelength conversion component after beam contraction. In the wavelength conversion sections, an 18 mm long type I phase-matched LiB_3O_5 (LBO) crystal with a cutting angle of 10.4 degrees is used for second harmonic generation (SHG) to produce a 532 nm laser, followed by a 10 mm long type II phase-matched LBO crystal with a cutting angle of 43.9 degrees being utilized for SFG to achieve a 355 nm laser. The 1064, 532 and 355 nm wavelength lasers are separately directed out by a pair of dichroic mirrors.

In this study, a 36 GHz bandwidth digital oscilloscope (LeCroy, MCM-Zi-A) and a high-speed photoelectric detector (Alphalas, UPD-35-UVIR-D) are used to detect the laser temporal waveform and RF spectrum. In addition, an optical spectrometer (Yokogawa, AQ6370) is employed to detect the optical spectrum. Moreover, an energy meter (Ophir, PE9-ES-C) is utilized for relative measurements of the output energy.

3. Experimental results and discussion

3.1. Burst-mode fiber seeder performance

In experiments, the laser system is initially scrutinized at a frequency of 1 GHz with an sinusoidal intra-burst pulse. In the fiber seeder, the CW laser is modulated into a pulse train by a high-bandwidth EOM. The characteristics of the pulse train are tested at the 1% port of the OC. The details of the pulse train shape are shown in Figure 2(a). The pulse train exhibits a sinusoidal shape, operating at a frequency

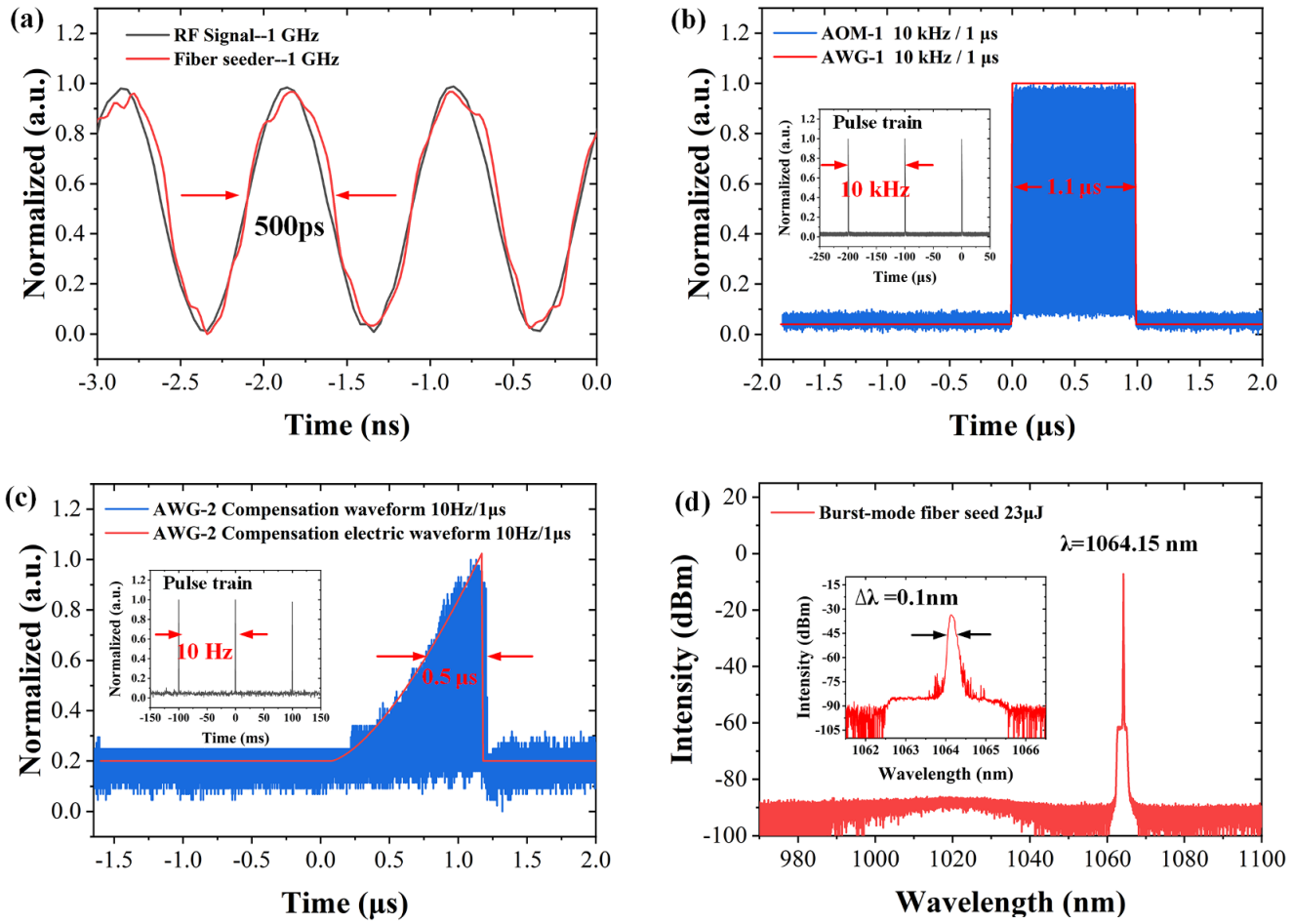

Figure 2. (a) The intra-burst pulse shape of the 1 GHz sine wave. (b) The AWG-1 pulse signal of 10 kHz/1 μs and the chopped pulse train of the microsecond burst-mode laser seed. (c) The AWG-2 pre-compensation signal waveform and the pre-compensated temporal shape of the burst-mode seed. (d) The spectrum of the burst-mode fiber seed.

of 1.0 GHz with a full width at half maximum (FWHM) of 500 ps. Meanwhile, the signal is not distorted compared to the RF signal due to the precision control of the EOM bias voltage. Through the first pre-amplifier the seed gained an average power of 300 mW. AOM-1 chopped the pulse train into a burst-mode laser; the temporal waveform of the burst-mode laser is shown in Figure 2(b). The rectangular pulse waveform from the AWG-1 signal is shown with a red line and the burst-mode pulse waveform following AOM-1 modulation is shown with a blue line. The envelope of the burst-mode pulse is a rectangular pulse that spans a width of 1.1 μs. The inset diagram shows that the burst pulse repetition rate is 10 kHz. Through the two pre-amplifiers the burst-mode pulse achieved a burst energy of 10.5 μJ. The AWG-2 pre-compensation waveform is based on the Frantz–Nodvik equations[30]. The output pulse shape is linked to the input pulse by a gain function:

$$I_{\text{output}} = I_{\text{input}} \cdot G(t), \tag{1}$$

where I_{output} is the output waveform and I_{input} is the input waveform. A simple exponential function gives $G(t)$[31]:

$$G(t) = 1 + (G_0 - 1) \cdot \exp\left(-\frac{E_{\text{out}}(t)}{E_{\text{sat}}}\right), \tag{2}$$

where E_{sat} is saturation energy and G_0 is the small-signal gain. They can be determined experimentally. Based on the inverse Frantz–Nodvik equation, a pre-compensation waveform has been calculated and is depicted in Figure 2(c); the red line represents the pre-compensation waveform generated by the AWG-2 signal, while the blue line shows the burst-mode pulse waveform following modulation by AOM-2. The envelope of the burst-mode pulse closely resembles the pre-compensated waveform produced by AWG-2. The inset diagram illustrates that the macro-pulse repetition rate has been reduced from 10 kHz to 10 Hz by the AOM-2 pulse picker. The burst energy of the burst-mode seed is approximately 23 μJ after the main amplifier. Figure 2(d) shows the burst-mode fiber seed spectrum, which indicates the center wavelength of the laser is 1064.15 nm and the nonlinear effects and ASE disappear. The inset diagram demonstrates that the 3 dB bandwidth of the spectrum is 0.10 nm. The maximum 3 dB bandwidth of the amplifier is within the optimal emission line of the Nd:YAG crystal[32].

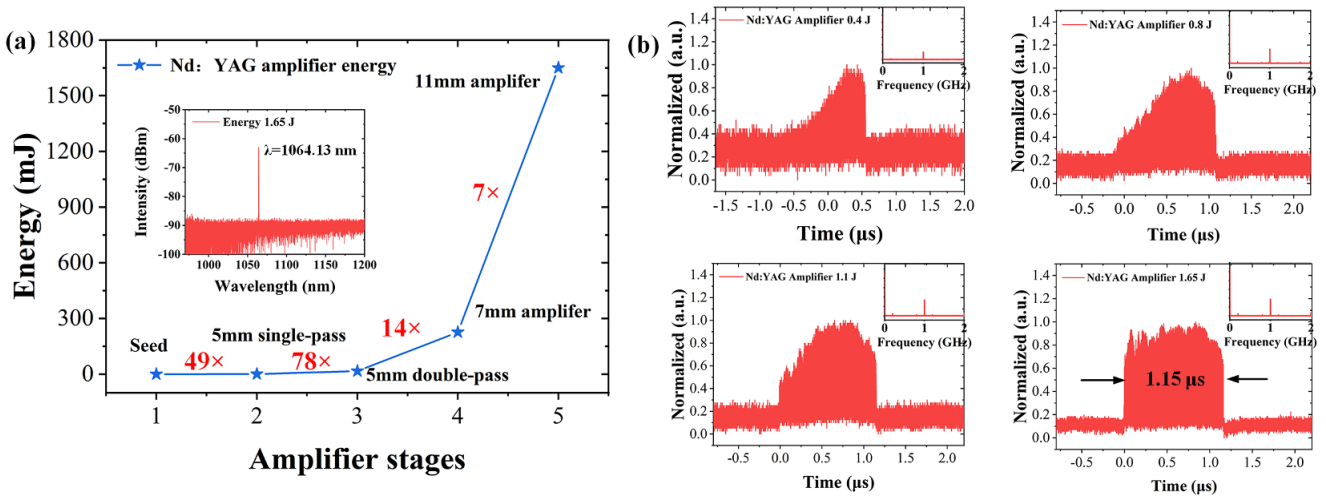

Figure 3. (a) Nd:YAG amplifiers vary in energy at different amplifiers. (b) Temporal waveform evolution of the burst-mode pulse laser at different energy values.

3.2. Nd:YAG amplifier output energy and temporal waveforms

The burst energy of the burst-mode fiber seed is further amplified by a multi-stage Nd:YAG amplifier. The multi-stage Nd:YAG amplifier consists of a one stage double-pass pre-amplifier and a two-stage one-pass main amplifier. The variation in burst energy at different amplification stages of the Nd:YAG crystal is shown in Figure 3(a). The burst energy of the fiber seed source is increased to 210 μJ after a single pass through the 5 mm Nd:YAG amplifier stage, resulting in an energy amplification factor of 49×. After a double-pass, the burst energy is further amplified to 16.4 mJ, yielding an energy amplification factor of 78×. The amplified burst-mode laser, after being expanded by a beam expander, is injected into the first 7 mm Nd:YAG rod main amplification stage. After this first main amplification stage, the laser energy increases to 226 mJ, resulting in an energy amplification factor of approximately 14×. Subsequently, the laser from the first stage of the main amplifier is expanded again by a beam expander before being injected into the second stage of the main amplifier. Following the 11 mm Nd:YAG amplification, the burst energy is further increased to 1.65 J, corresponding to a peak power exceeding 3 MW, achieving an energy amplification factor of 7×. The Figure 3(a) insert diagram shows the spectrum at the maximum energy of the amplifier. The spectrum shows the center wavelength is 1064.13 nm and the ASE and nonlinear effects do not appear, which is beneficial to improve the conversion efficiency of second harmonics. The Figure 3(b) demonstrates the temporal pulse waveform of the Nd:YAG crystal at different burst energy levels of 0.4, 0.8, 1.1 and 1.65 J. At the burst energy level of 0.4 J, it can be observed that the front edge of the temporal pulse waveform is depressed, with an FWHM of approximately 0.5 μs. The temporal pulse waveform is similar to that of the burst-mode fiber seed, indicating that the amplified energy at this level does not reach the gain saturation threshold of the amplifiers. As the energy increases, the front edge of the waveform gradually rises because of the gain saturation effects. When the amplifier energy reaches 1.65 J, the waveform becomes flat-topped and the shape of the pulse takes on a rectangular envelope with a pulse width of 1.15 μs.

3.3. Characteristics of the high-power UV burst-mode laser

Here we describe the high-power 1064 nm burst-mode pulse laser output high-power UV burst-mode pulse laser by SHG and THG. Double- and triple-frequency LBO crystals are employed for 532 and 355 nm wavelength conversion. The temperature of the double- and triple-frequency LBO crystals is set to 45ºC for higher wavelength conversion efficiency. We measured the output energy of the high-power UV burst-mode pulse laser. Firstly, after SHG, a burst energy of 400 mJ is achieved at 532 nm, resulting in an SHG efficiency of 25% from 1064 to 532 nm. Following this, we obtained a burst energy of 152 mJ at 355 nm, corresponding to a peak power of over 300 kW. The SFG efficiency of approximately 38% is from 532 to 355 nm. To assess the stability of the laser system, we continuously monitor the burst-mode pulse energy at wavelengths of 532 and 355 nm over a period of 10 minutes, recording burst energies of 400 and 152 mJ, respectively. The measurement results are presented in Figure 4(a), which shows that the root mean square (RMS) fluctuations in energy for the 532 and 355 nm outputs are 1.5% and 1.25%, respectively. This indicates that the UV burst-mode laser amplifier maintains good energy stability. In addition, we measured the spectrum of the UV burst laser. The results presented in Figure 4(b) indicate a central wavelength of 355.12 nm along with a 3 dB spectral width of 1.5 nm.

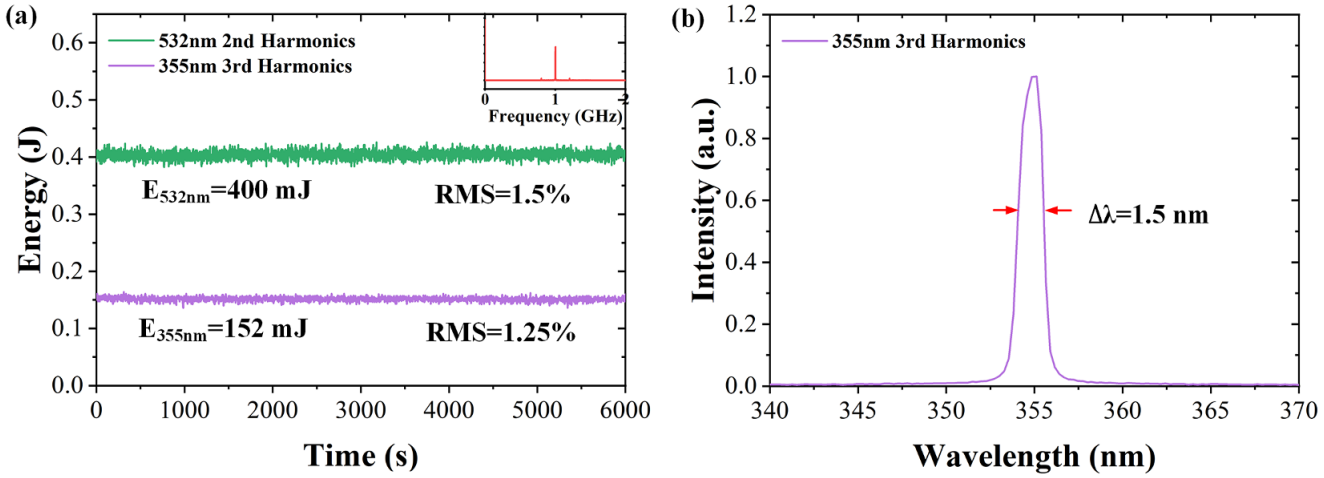

Figure 4. (a) The energy stability of the UV laser is assessed over a 10-minute interval. (b) The spectrum of the UV burst-mode laser at maximum output energy.

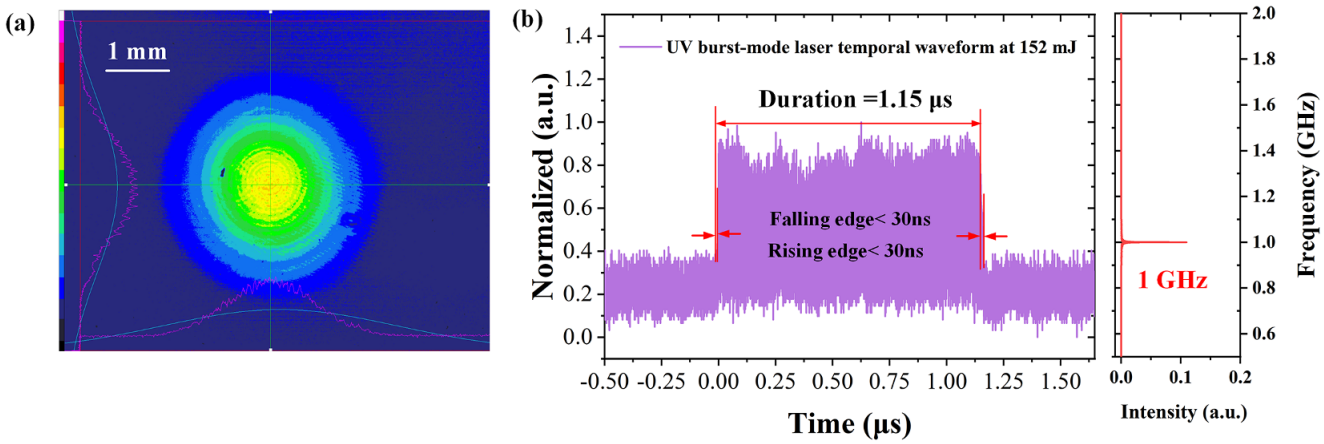

Figure 5. (a) The spatial profile of the UV burst-mode laser at 152 mJ (over 300 kW peak power). (b) The temporal waveform of the UV burst-mode laser at 152 mJ.

The beam profiles of the UV pulse laser are measured using a beam profiler (Coherent, LaserCam HR II). The spatial profile of the high-power UV burst-mode laser, operating at 152 mJ (~300 kW peak power), is displayed in Figure 5(a). A near-Gaussian profile has been achieved, demonstrating a symmetrical distribution with a beam size of approximately 3.3 mm at an 86% Gaussian fit. The temporal waveform of the UV burst-mode pulse laser at 300 kW peak power is represented in Figure 5(b). The macro-pulse envelope indicates a nearly rectangular profile with a pulse width of 1.15 μs with both the rising and falling edges measuring less than 30 ns. The macro-pulse envelope is relatively stable in the third harmonic conversion process, and the pulse waveform and pulse width are basically consistent with the Nd:YAG amplifier, which will be conducive to the output of more uniform microwave energy in PMT.

We measured the tuning frequency of the intra-burst pulse at the maximum power at the 355 nm laser output port. It is worth noting that in the measurement process, due to the small energy threshold of the injected light of the detector, the coupling angle of the multi-mode fiber needs to be adjusted to control the coupling energy to avoid detector saturation and damage. In the experiment, by varying the signal generator frequency in the burst-mode fiber seed, the intra-burst frequency of the UV burst-mode laser can be adjusted in real time. Meanwhile, when measuring the UV laser spectrum and signal-to-noise ratio (SNR), the multi-mode fiber coupling angle is adjusted so that the energy incident on the detector is essentially the same, ensuring that the detector compares SNRs at different intra-burst pulse frequencies with the same photoelectric response. Figure 6(a) displays the RF spectrum of the UV burst-mode pulse laser operating at different intra-burst frequencies, ranging from 1 to 10 GHz in 1 GHz increments. The SNR exceeds 40 dB, indicating that nearly all of the power is effectively utilized for generating alternative microwave signals when the high-power UV burst-mode is applied in PMT. Figure 6(b) shows the tunable sinusoidal intra-burst pulse duration, which ranges from 100 ps to 1 ns, corresponding to various intra-burst frequencies of 1–10 GHz. The intra-burst pulse

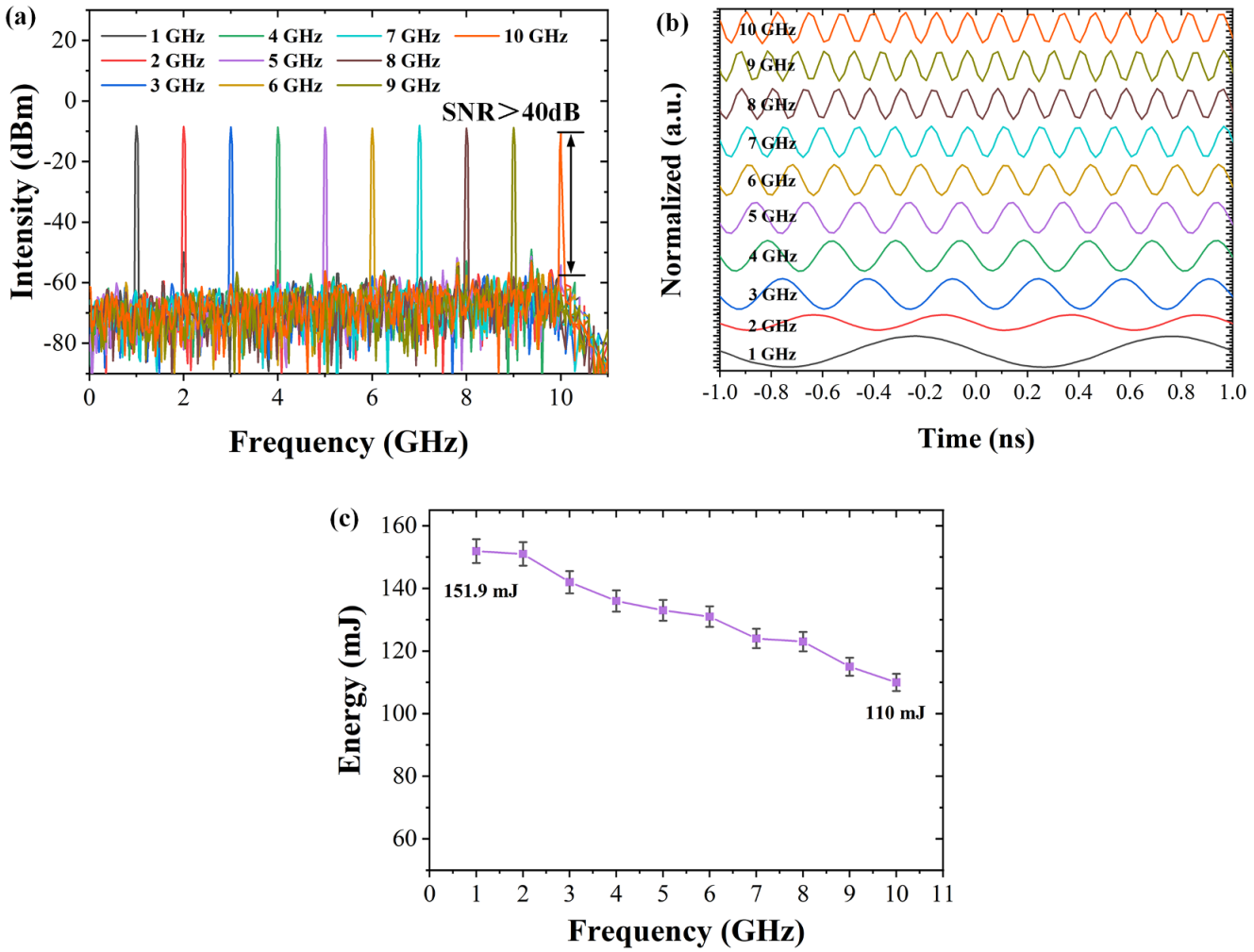

Figure 6. (a) The UV burst-mode laser features an intra-burst pulse frequency that is adjustable across the 1–10 GHz spectrum. (b) The sinusoidal intra-burst pulse train at various intra-burst frequencies of 1–10 GHz. (c) The output energy at different intra-burst frequencies of 1–10 GHz.

exhibits a sinusoidal waveform with minimal distortion following laser amplification and third harmonic conversion, which will facilitate the generation of microwaves across different frequency bands in the PMT. Figure 6(c) shows the output energy at different intra-burst frequencies (energy fluctuation of 2.5%), which indicates that the UV laser output energy decreases with increasing intra-burst frequency. At 1 GHz intra-burst frequency, the energy is 151.9 mJ, while at 10 GHz intra-burst frequency, the energy decreases to 110 mJ. In PMT applications, in order to ensure that the same microwave power is output at high frequencies, we can compensate by increasing the DC bias voltage[13].

4. Conclusion

In summary, we have successfully demonstrated a microsecond duration MOPA configuration burst-mode pulse laser system that provides a GHz-adjustable intra-burst pulse frequency. The laser operates with a duration of 1.15 μs and a repetition rate of 10 Hz. The seed laser is a CW laser with a narrow linewidth at 1064 nm. The CW laser is modulated into a pulse train with frequencies ranging from 1 to 10 GHz by a high-bandwidth EOM. AOM-1 chops this pulse train to produce a burst laser with a burst duration of 1.1 μs and a macro-pulse repetition rate of 10 kHz. AOM-2 is utilized not only to create a compensation pulse waveform with a low front and high back to counteract the gain saturation effect caused by laser amplification, but also to reduce the macro-pulse repetition rate of the burst-mode laser from 10 kHz to 10 Hz. A customized three-stage Nd:YAG amplifier increased the burst energy of the fiber seed laser to 1.65 J, along with a peak power of 3.3 MW. Through third harmonic conversion, we achieved a peak power of over 300 kW at 355 nm. The high-power UV burst-mode laser exhibits a burst duration of 1.15 μs with a nearly rectangular envelope. The beam profiles of the UV laser display a near-Gaussian profile with a beam size of approximately 3.3 mm. The energy RMS is 1.25%, indicating high energy stability. In addition, the intra-burst pulse frequency of the UV burst

laser is adjustable from 1 to 10 GHz. The high-peak-power microsecond UV burst-mode pulse laser can be directly used as a light-driven source in large-bandwidth/high-power MWP systems, providing a long-pulse-width and high-peak-power laser while significantly improving the system's multi-parameter adjustment capability and adaptability.

Acknowledgements

This work was supported by the National Natural Science Foundation of China (Grant Nos. 62071477 and 62101577) and the Postgraduate Scientific Research Innovation Project of Hunan Province (Grant No. QL20230011). The authors are particularly grateful to Rongling Wei of Beijing Zhuolei Laser Technology Co., Ltd for her help in fiber seed research and development, and Wei Wang for his support in commercial amplifier construction technology and research and development.

References

1. M. A. Murzakov, N. N. Evtikhiev, N. V. Grezev, D. M. Kataev, and A. S. Shchekin, Laser Phys. Lett. **21**, 025601 (2024).
2. H. Le, T. Karkantonis, V. Nasrollahi, P. Penchev, and S. Dimov, Appl. Phys. A **128**, 711 (2022).
3. H. Zhang, X. Liu, Y. Li, W. Wu, Y. Gu, and T. Zhang, J. Biophotonics **15**, e202200197 (2022).
4. Z. Qian, A. Mordovanakis, J. E. Schoenly, A. Covarrubias, Y. Feng, L. Lilge, and R. S. Marjoribanks, Biomed. Opt. Express **5**, 208 (2013).
5. V. Danilov, A. Aleksandrov, S. Assadi, J. Barhen, W. Blokland, Y. Braiman, D. Brown, C. Deibele, W. Grice, S. Henderson, J. Holmes, Y. Liu, A. Shishlo, A. Webster, and I. N. Nesterenko, Phys. Rev. Spec. Top. Accel. Beams **10**, 053501 (2007).
6. K. Sakaue, M. Washio, S. Araki, M. Fukuda, Y. Higashi, Y. Honda, T. Omori, T. Taniguchi, N. Terunuma, J. Urakawa, and N. Sasao, Rev. Sci. Instrum. **80**, 123304 (2009).
7. L. Wang, X. Chu, M. Yi, J. Yao, T. Xun, and H. Yang, IEEE Trans. Electron Devices **69**, 5028 (2022),
8. X. He, B. Zhang, S. Liu, L. Yang, J. Yao, Q. Wu, Y. Zhao, T. Xun, and J. Hou, High Power Laser Sci. Eng. **9**, e13 (2021),
9. Y. Gu, J. Yao, N. Yue, M. Yi, L. Wang, T. Xun, H. Yang, J. Liu, X. Ge, and J. He, IEEE J. Electron Devices Soc. **12**, 256 (2023).
10. S. Liu, B. Zhang, Y. Bu, D. Zhao, X. Zhu, L. Yang, and J. Hou, High Power Laser Sci. Eng. **11**, e81 (2023).
11. X. Chu, J. Meng, H. Wang, D. Zhu, B. Deng, and Y. Cui, IEEE Trans. Electron Devices **71**, 4253 (2024).
12. Z. Feng, C. Luan, L. Xiao, Y. Li, H. Sha, X. Sun, X. Chen, X. Xu, and H. Li, IEEE Trans. Electron Devices **70**, 627 (2023).
13. X. Chu, T. Xun, L. Wang, H. Yang, J. Liu, J. He, and J. Zhang, IEEE Electron Device Lett. **43**, 1013 (2022).
14. J. Zhang, D. Zhang, Y. Fan, J. He, X. Ge, X. Zhang, J. Ju, and T. Xun, Phys. Plasmas **27**, 010501 (2020).
15. F. J. Ortega-Gonzalez, D. Tena-Ramos, M. Patino-Gomez, J. M. Pardo-Martin, and D. Madueno-Pulido, IEEE Trans. Microwave Theory Techn. **61**, 3712 (2013).
16. W.-R. Fang, W.-H. Huang, W.-H. Huang, J.-W. Li, C. Fu, L.-L. Wang, T.-W. He, and Y. Cao, IEEE Microwave Wireless Components Lett. **30**, 884 (2020).
17. J. Capmany, J. Mora, I. Gasulla, J. Sancho, J. Lloret, and S. Sales, J. Lightwave Techn. **31**, 571 (2013).
18. D. Marpaung, J. Yao, and J. Capmany, Nat. Photonics **13**, 80 (2019).
19. X. Niu, Q. Wu, B. Wang, J. Yao, X. Chu, M. Yi, Y. Gu, L. Wang, T. Xun, and H. Yang, IEEE Photonics J. **15**, 5500407 (2023).
20. G. N. Saddik, R. S. Singh, and E. R. Brown, IEEE Trans. Microwave Theory Techn. **55**, 1431 (2007).
21. C. Huang, C. Deibele, and Y. Liu, Opt. Express **21**, 9123 (2013).
22. J. Zhang, D. Li, W. Cheng, and H. Zhang, Opt, Laser Technol. **158**, 108848 (2023),
23. T. Xun, X. Niu, L. Wang, B. Zhang, J. Yao, Y. Yu, H. Yang, J. Hou, J. Liu, and J. Zhang, Chin. Opt. Lett. **22**, 012501 (2024),
24. Y. Gu, X. Niu, T. He, M. Yi, J. Yao, L. Wang, T. Xun, and J. Liu, Proc. SPIE **13179**, 1317909 (2024).
25. H. Yu, J. Zhang, Y. Qi, L. Zhang, S. Zou, L. Wang, and X. Lin, J. Lightwave Techn. **33**, 1761 (2015).
26. S. C. Li, T. L. Huang, Y. H. Hsieh, H. C. Liang, K. F. Huang, and Y. F. Chen, Opt. Lett. **45**, 61 (2019).
27. L. Han, T. Wang, R. Liu, W. Ma, Y. Zhao, Q. Fu, and H. Jiang, IEEE Photonics J. **12**, 7101508 (2020).
28. S. Cai, B. Wu, Y. Shen, and P. Jiang, Laser Phys. **30**, 095101 (2020).
29. K. H. Wei, R. H. Wen, and Y. Guo, Laser Phys. Lett. **13**, 045102 (2016).
30. L. M. Frantz and J. S. Nodvik, J. Appl. Phys. **34**, 2346 (1963).
31. D. N. Schimpf, C. Ruchert, D. Nodop, J. Limpert, A. Tünnermann, and F. Salin, Opt. Express **16**, 17637 (2008).
32. C. Guo, Q. Bian, C. Xu, J. Zuo, Y. Bo, Z. Wang, Y. Shen, N. Zong, H. Gao, Y. Liu, D. Cui, Q. Peng, and Z. Xu, IEEE Photonics J. **8**, 1504908 (2016).